Optical, thermal, and bit-writing analysis of a directly coupled plasmonic waveguide for heat-assisted magnetic recording

FRANK BELLO,[1,4] **DANIEL WOLF,**[2] **GREGORY J. PARKER,**[2] **CHRISTOPHER WOLF,**[2] **ALEXANDER KRICHEVSKY,**[2] **FENGHUA ZONG,**[2] **NICOLÁS ABADÍA,**[3] **AND JOHN F. DONEGAN**[1,5]

[1] *School of Physics, CRANN, and AMBER, Trinity College, Dublin 2, Ireland*
[2] *Western Digital Corporation (WDC), San Jose, CA 95119, USA*
[3] *School of Physics and Astronomy and Institute for Compound Semiconductors, Cardiff University, Cardiff CF24 3AA, UK*
[4] *bellofr@gmail.com*
[5] *jdonegan@tcd.ie*

Abstract: We investigate the energy conversion process and subsequent thermal and bit-writing performance of a plasmonic near-field transducer (NFT) under steady-state operation within heat-assisted magnetic recording (HAMR) devices. The NFT is composed of metal-insulator-metal (MIM) layers that are designed to localize heating and produce optimal thermal gradients in order to relieve parasitic heating effects in the NFT. The thin-film MIM structure confines the electromagnetic energy in the down-track direction while cross-track confinement is achieved by tapering the insulator feature of the MIM. A comparative analysis using Gold and a number of novel Au alloys is undertaken. Modeled performance shows excellent thermal spot confinement $(50 \times 50 \text{ nm}^2)$ of temperatures above 650 K at an input laser power of 830 nm of less than 5 milliwatts. In addition, micromagnetic simulations using a stochastic Landau-Lifshitz-Bloch equation yield excellent signal to noise ratio with minimum jitter of under 2 nm when recording.

1.   Introduction

The present approach to heat-assisted magnetic recording (HAMR) is based on an integrated head design containing a diode laser coupled to an optical waveguide to deliver a photonic mode to excite the NFT [1–3]. The photonic mode is resonant with a NFT plasmonic mode, which has a wavelength many times smaller than the free space wavelength of light, and therefore produces subdiffraction focusing [4,5]. The NFT in turn creates a nanoscale localized hot spot within the media that is in the immediate vicinity of an external write pole [6]. It is essential for the extended lifetime of the head to localize the heating to the desired area, and also to keep the NFT as cool and thermally stable as possible while heating the recording media above its Curie point [7]. To achieve this, we herein focus on a NFT design intended to be excited under direct fire from a dielectric waveguide. Figure 1 illustrates the conceptual difference between a commonly used evanescent coupling approach [8] [Fig. 1(a)] and a direct coupling method [Fig. 1(b)]. In both cases, the energy is predominantly contained inside the high refraction index core of the dielectric waveguide [9,10], while the exponentially decaying tails extend into a lower-index cladding. The difference is in the coupling method to the NFT. For evanescent coupling, it is the exponentially decaying tail of the photonic mode within the core that excites a plasmonic mode in the NFT. The bulk of the energy passes by and reaches the air-bearing surface (ABS) where the photonic mode undergoes significant reflection from the media. The reflected wave returns to the laser as unwanted feedback causing instability, while the transmitted part creates parasitic heating in the media limiting the bit-writing performance. Although significant reflection can

also occur using the direct-fire method, the NFT is in-line with the dielectric core and therefore reduces unwanted, parasitic heating.
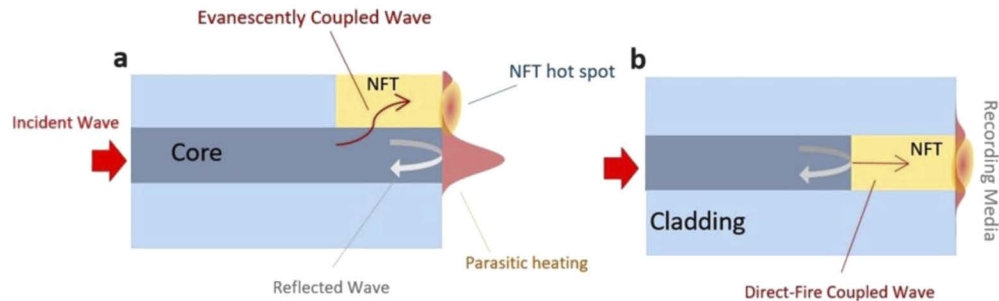
Fig. 1. (a) Schematic demonstrating the evanescent coupling of a dielectric waveguide mode with a plasmonic NFT mode. The evanescent tail of the mode within the dielectric core is the source of excitation of the plasmonic mode. The rest of the energy may be reflected back to the laser or transmitted to the recording medium causing unwanted heating and possible damage away from the bit-writing region. Hence, additional components need to be added to avoid parasitic heating (red peaks). (b) Directly coupling the photonic mode within the core to the NFT allows energy to be dissipated via heatsinking of the device while reducing the amount of the reflected wave which reaches the recording media.

2. Results and discussion

2.1. Near field transducer and plasmonic behavior

The NFT investigated is intended for steady state operation, i.e. when the laser's field is unchanging in time, in HAMR devices (Schematic in Fig. 2). During HAMR operation, temperatures of the recording medium need to surpass the Curie temperature of the recording medium ($\approx$ 650-700 K for FePt) and produce very large temperature gradients (30-40 K/nm in total magnitude). This can inadvertently heat the nearby NFT, which is positioned only 9 nm from the recording media layer (standard for HAMR devices), to temperatures up to or exceeding 400 K for roughly a few ns [1]. A write pole is also integrated on top of the NFT, which further contributes to thermal insulation, and thus additional heatsinking material needs to be included in order to reduce its temperature (see Section 3 for a complete list of dimensions, placement and media parameters). Pure Au, which is initially used in simulations, may become malleable and prone to protrusion under such conditions [11,12], therefore our study includes the thermal and magnetic performance when using various Au alloys within the NFT in the following section. Alloying has been a traditional method of strengthening Au materials in areas such as jewelry. Here we must maintain the thermal conductivity and the plasmonic response.

The photonic waveguide is designed for single mode operation, which excites a TM-polarized surface plasmon (SP) mode within the metal-insulator-metal NFT [8]. As shown in Fig. 3, the electric and magnetic field profiles are that of an antisymmetric, high-energy SP mode [13,14]. This NFT is able to retain the bulk of the power in the insulator layer rather than the metallic component which may be advantageous compared to designs where it is contained within metallic layers [15]. This enables Au parts of the nanostructure to be replaced with alloys that may not have the same plasmonic performance, and therefore as high an optical efficiency as Gold, however they could significantly increase the thermal stability and hardness of the NFT. An antireflective (AR) trench composed of SiO_2 is included in the design to improve coupling efficiency between the plasmonic and a photonic mode excited by the fundamental TM mode with wavelength 830 nm in a SiN core [15]. It functions analogously to a quarter- wavelength
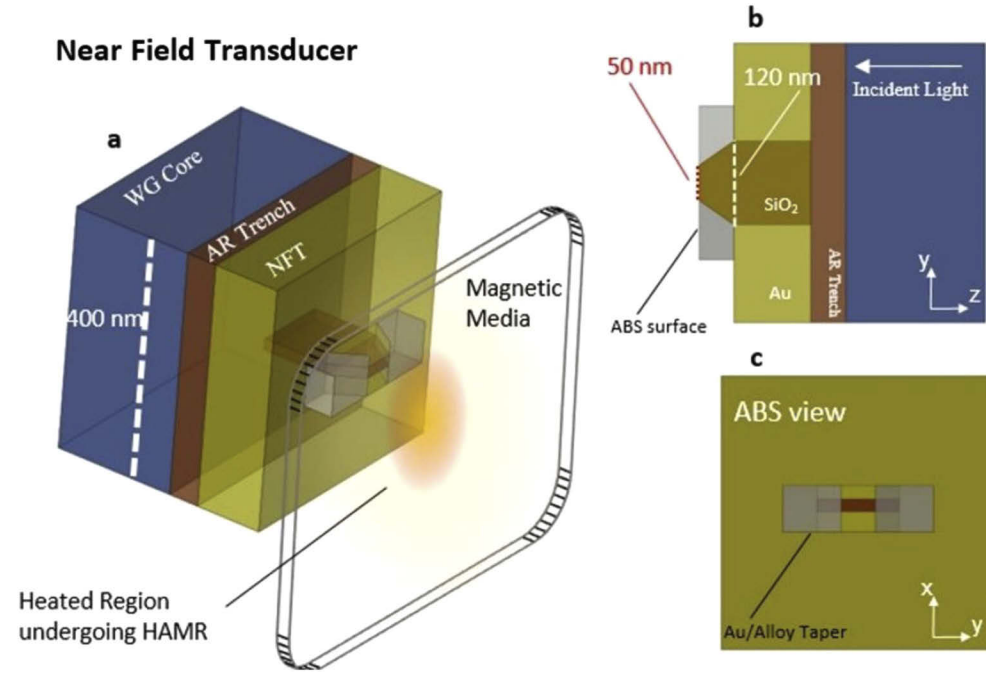
Fig. 2. (a, b, c) Minimal model and cross-sections of the plasmonic waveguide NFT composed of a 18 nm thick insulator core surrounded by Au (metal-insulator-metal resonator). An antireflective (AR) trench is added to reduce feedback between the dielectric waveguide and the NFT. The short taper reduces thermal spot profiles while the smaller section at the air-bearing surface allows for placement of a magnetic write pole or encasement. Au alloys were placed on both sides of the short tapered section (gray material) of the insulator layer in order to improve thermal efficiency near the air-bearing surface (ABS).

coating that in this case matches the wavelength of the input photonic mode with that of the NFT's excited plasmonic mode.

There is relatively high loss due to the metallic components of the device that limits the length of the NFT in the direction of propagation to 160 nm. This is notably shorter than the surface plasmon wavelength, $\lambda_{sp} = \frac{\lambda_0}{n_{eff}} \approx 380$ nm, with the effective index derived from the Fabry-Perot resonance relation [16],

$$n_{eff} \approx \frac{\pi}{k_0 \cdot \Delta L_E} = \frac{\lambda_0}{2(|E_{p1}^2| - |E_{p2}^2|)} \tag{1}$$

where the values $E_{p1(2)}$ refer to the first and second positions along the waveguide showing a peak in the electric field magnitude. Tapers of this length, e.g. 160-380 nm, significantly reduce the amount of power delivered to the media due to scattering. Hence, only a very short taper of 50 nm in the direction of propagation was placed at the tip of the plasmonic element to reduce the size of the heated area in the media. This was shown to further increase the areal density in a HAMR hard drive [17,18].

2.2. Thermal behavior of near field transducer and recording media

Next, it is essential to analyze the light-heat energy conversion that undergoes within the apparatus. Figure 4 demonstrates the temperature and thermal gradients obtained from the resistive heating (power loss) in the magnetic media. Results were obtained from finite-element simulations (see Section 3 for details) where thin film parameters for FePt, which is our recording medium,
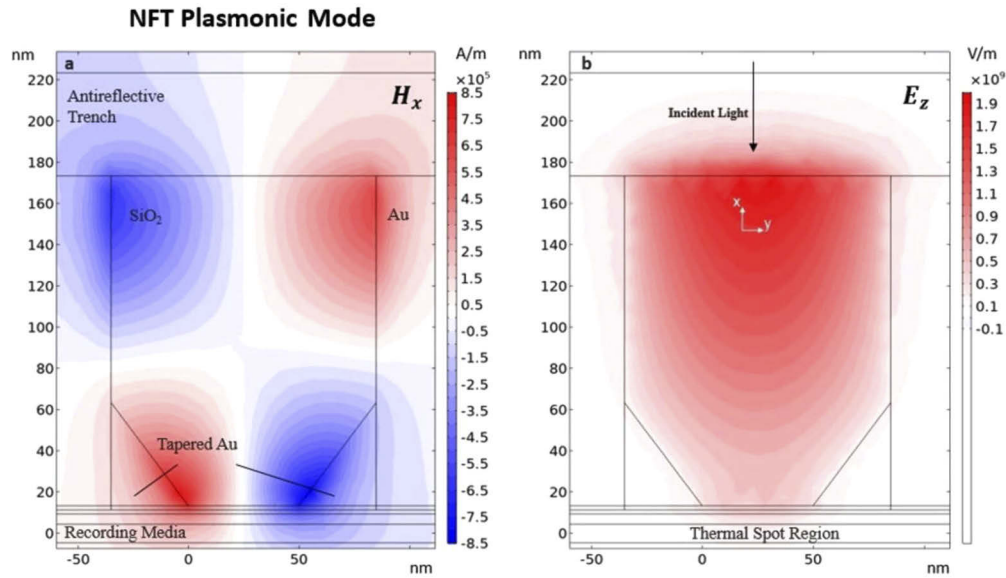
Fig. 3. Planar cross-section [similar to Fig. 2(b)] taken thru the center of insulator layer of the MIM resonator showing excitation of an antisymmetric SP mode with the magnetic field component (H_x) in (a) and the electric field component (E_z) in (b) which both dominate in magnitude compared to other components. The 0-point on the x-axis is the same 0-point in Fig. 4 while the 0-point on the y-axis corresponds to the center of the magnetic recording layer.

were used in the calculation (see Section 3 for dimensions and material parameters). One can ultimately control the recorded track width over which data is stored at the nanometer scale by adjusting the NFT input power and therefore heating. Manipulation of the NFT power will also be able to mitigate any unexpected heating if TE portions of input light exist in experiments. This is vital for maximizing areal bit densities, i.e. cross × down track region, in magnetic recording devices that must be less than 50×50 nm^2 to meet industry standards of storage densities of 1 Tb/in^2 or greater. In addition, thermal gradients over 10 K/nm are desired in order to not overwrite adjacent bits with parasitic heating.

Table 1 contains a comparative analysis of the thermal performance [6] when replacing various components of the NFT with Au alloys that have a number of desired properties, such as a larger thermal conductivity than pure Au as well as increased hardness [19,20]. As listed, we have replaced the entire metallic component with alloys, followed by a capping layer at the ABS surface, and then the tapered components at the ABS surface (highlighted in gray in Fig. 2). The materials with the overall best thermal performance are highlighted in green. In particular, the change in media temperature compared to that of the Gold ($\frac{\Delta T_{media}}{\Delta T_{Au}}$) is shown, which is larger than many antenna-based designs investigated for HAMR, though smaller compared to a number of aperture-based designs, e.g. C- and bowtie, which may obtain values well over 20 [2,6]. However, for HAMR, it is sufficient to have $\frac{\Delta T_{media}}{\Delta T_{Au}} < 10$ to ensure bit writing while keeping the temperature of Au under 400 K, at which point Au is known to become significantly malleable [21]. Herein, we demonstrate the ability to keep Au temperatures closer to 350 K for HAMR, which will greatly reduce the softness of the metal and any anticipated thermal expansion of the thin film structure.

Of further importance are the down and cross track temperature gradients; imperative for maximizing areal density, consistency in bit size, and speed of bit-writing. Aperture-based NFT designs such as E- and C-types as well as 'lollipop' antennas have maximum, theoretical

Light to Heat Energy Conversion
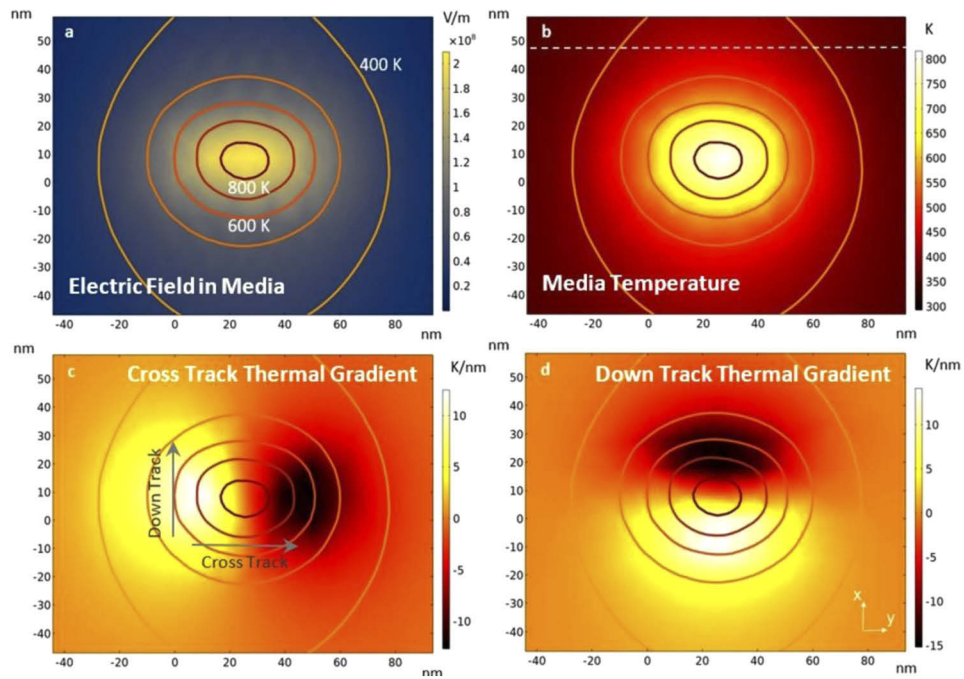
Fig. 4. Planar cross-section taken from the center of the magnetic media layer showing profiles for the normalized electric field (a), the temperature (b), along with the cross (c) and down (d) track temperature gradients. All profiles have the same temperature contours superimposed on them. The position of the NFT's insulator (corner) is marked by the 0-point and the position of the tip of the write pole is marked with the dashed line shown in (b).

Table 1. Thermal performance parameters.

WD/TCD Patented NFT Design	$\Delta T_{Media}/\Delta T_{Au}$	Max Temp Au	Max Temp FePt	Max Down Track Gradient	Max Cross Track Gradient
(Au, n=0.17) $P_{in} = 7.25\ mW$	5.25	394 K	823 K	14.4 K/nm	11.8 K/nm
(Au, n=0.06) $P_{in} = $ **4.7 mW**	**8.52**	356 K	830 K	15.0 K/nm	12.5 K/nm
(AuAg$_7$ ordered) $P_{in} = 5.2\ mW$	**8.46**	356 K	826 K	15.6 K/nm	13.0 K/nm
Au + Capping layer at ABS (2 nm)					
(Pd) $P_{in} = 5.1\ mW$	5.89	384 K	829 K	14.5 K/nm	12.9 K/nm
(Au$_{0.5}$Pd$_{0.5}$) $P_{in} = 5.5\ mW$	6.86	371 K	828 K	13.5 K/nm	11.6 K/nm
(Au$_{0.1}$Pt$_{0.9}$) $P_{in} = $ **4.7 mW**	**8.51**	356 K	829 K	15.3 K/nm	13.2 K/nm
Replacement of tapered section					
(Au$_{0.175}$Ag$_{0.875}$ random) - $P_{in} = 4.9\ mW$	**8.60**	355 K	826 K	14.7 K/nm	12.8 K/nm
(Au$_{0.75}$Cu$_{0.25}$ random) - $P_{in} = 5.0\ mW$	**8.52**	356 K	830 K	14.7 K/nm	12.7 K/nm

thermal gradients reported of roughly 7 K/nm [6]. Antenna-based, evanescently coupled designs have reported the largest thermal gradients, experimentally or theoretically, of roughly 14-15 K/nm [1,22]. In addition, non-descript near-field transducers were reported to experimentally demonstrate gradients ranging between 8-10 K/nm [23,24]. We are able to match these maximum gradients within the FePt media, with thermal gradients improving within the media when using a number of the Au-alloys within the NFT whose parameters are obtained from [20,25]. At the same time, we maintain maximum temperatures in the recording layer above 800 K and minimize temperatures in the NFT below 400 K. This is critical to reduce parasitic heating and prevent adjacent bits from being overwritten during the recording process.

Furthermore, alloys composed of AuPd or AuPt were able to meet the performance requirements for HAMR when used as capping layers on the surface of the NFT. The anticipated hardness of these alloys compared to pure Gold will help reduce thermal expansion and burnishing of the NFT, which may come into contact with the media/debris [26]. Hence, the use of Au alloys is advantageous in keeping NFTs closer to room temperature and making the write head less prone to mechanical failures. Thermal gradients presented in Table 1 compare well with other NFT designs, while surpassing many of those previously reported upon such as bowtie, C-aperture, or E-antenna designs [3,6]. Reported indices for pure Au vary widely for a wavelength of 830 nm; here we have chosen to model a theoretically derived index of n=0.06 [20] and an approximation of reported experimental values of n=0.17 [1–3]. It is noteworthy that the lower index for Au (n=0.06 compared to n=0.17) leads to a higher retention of energy within the insulator layer and improved performance as shown in Table 1.

2.3.   Magnetic behavior within recording media

Ultimately, throughout the analyzation of light-heat-magnetic energy conversion it is the bit-writing performance that must be optimized while maintaining cooler temperatures for a suitable lifetime of the apparatus. The magnetization pattern produced in the media using pure Au for the NFT is shown in Fig. 5, which was attained by solving the Landau-Lifshitz-Bloch (LLB) equation for a strip of media roughly 200 nm wide by 12000 nm long [27,28] (See Section 3 for details). The magnetization is altered with a magnetic write width (MWW) of approximately 40 nm in the cross-track direction with sample SNR and jitter calculations shown for the case of pure Au. The SNR results range from roughly 14.5-16 dB and a minimum jitter of roughly 2 nm, which is desired for HAMR [29], is achievable near the center of the recorded bit. Both of which compare well to previous values reported for HAMR devices where we notice state-of-the-art jitters ranging between 1.6-2.0 nm with SNRs of roughly 15.0-16.0 dB in evanescently-coupled, lollipop NFTs [29–32]. However, we noticed lower temperature gradients being reported if jitter was superior, and note that all previous NFT designs in this analysis used only pure Au.

Table 2 summarizes the bit-writing performance we see for the best cases presented in Table 1. In particular, we show the jitter for a given maximum temperature in the FePt media, along with the width of the bit (MWW) and signal-to-noise ratio (SNR). Jitters around or below 2 nm are desired with SNR ratios circa 15 dB or above with results listed in order of lowest jitter and highest SNR achievable. Of note, a minimum jitter of 2.01 nm and SNR of 15.9 dB is attainable even using Au-alloys for NFT capping layers composed of harder $Au_{0.5}Pt_{0.5}$. This is in addition to the excellent cross and down track temperature gradients and Au temperatures well below 400 K when using $Au_{0.1}Pt_{0.9}$ for capping. The values for jitter and SNR were selected/calculated over a range of 9 peak temperatures, i.e. 650:25:850. The maximum temperature for which the optimal jitter and SNR was achieved is estimated between 725-750 K. Assuming Curie temperatures around 700-750 K for the FePt layer would allow Au temperatures in the NFT to be kept well below 350 K for many of the cases presented in Table 1 (highlighted in green). This will significantly improve the thermo-mechanical stability and lifetime of NFTs compared to those with Au temperatures approaching 400 K [6].

OSA *CONTINUUM*
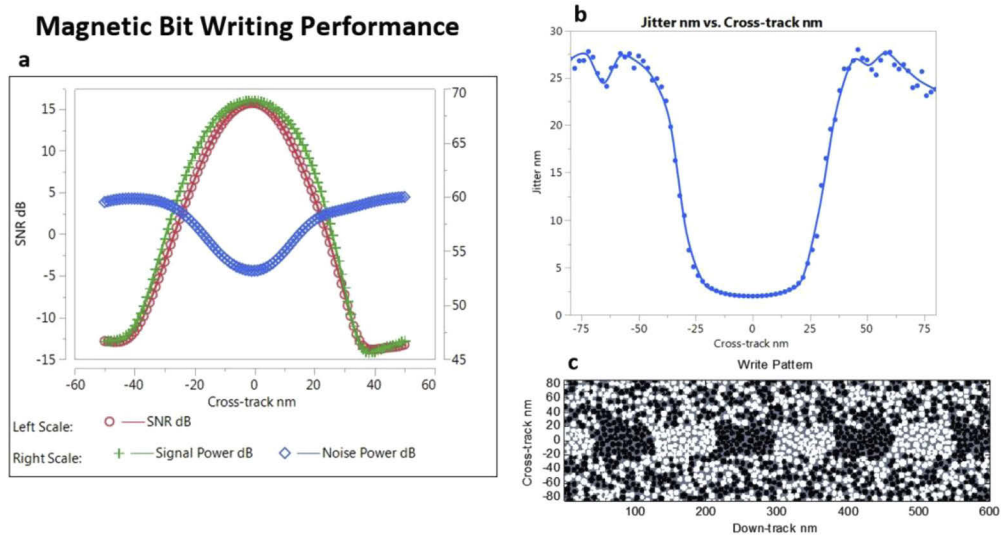
Fig. 5. (a) Sample signal (green) and noise power (blue) used to calculate SNR (red) in the cross- track direction for the case of pure Au (n=0.06) used for the metallic components of the NFT. (b) Jitter plotted along the cross-track position. (c) Corresponding write pattern on media with white grains pointed up, black grains down and gray area non-magnetic material.

Table 2. Magnetic performance parameters.

	Jitter (nm)	T_{max} media (K)	MWW (nm)	SNR(dB)
(Au, n=0.06)	1.96	750	41.6	16.0
(Au$_{0.1}$Pt$_{0.9}$)	2.01	750	41.7	15.9
(AuAg$_7$ ordered)	2.00	725	39.5	14.7
(Au, n=0.17)	2.17	725	40.1	14.8
(Au$_{0.75}$Cu$_{0.25}$ random)	2.16	725	38.9	14.6
(Au$_{0.175}$Ag$_{0.875}$ random)	2.24	750	40.8	15.1
(Au$_{0.5}$Pd$_{0.5}$)	2.31	725	40.9	14.9

3.   Simulation methods

In order to calculate the optical and thermal data, finite-element simulations of the waveguide, NFT, and media were performed using Comsol software [33]. Simulations containing roughly 1×10^6 data points were tested until we found a consistent error of 2-3% in successive runs, similar to Ref. [1]. The resistive heating (W/m^3) retrieved throughout the apparatus from the steady state solution of the Helmholtz equation was the heat source when solving for the thermal diffusion equation [34]. The simulations included the entire structure; waveguide, NFT, and thin film media as shown in Fig. 6. Boundary conditions for the simulations included an SiO$_2$ cladding of the NFT and waveguide with dimensions of 2.8 µm, 5.0 µm and 1.5 µm (x, y, z) where perfect electric conductors (PECs) were applied to the outermost boundaries. All dimensions and material parameters are shown in Tables 3 and 4 with parameters for Au alloys taken from Refs. [20,25].
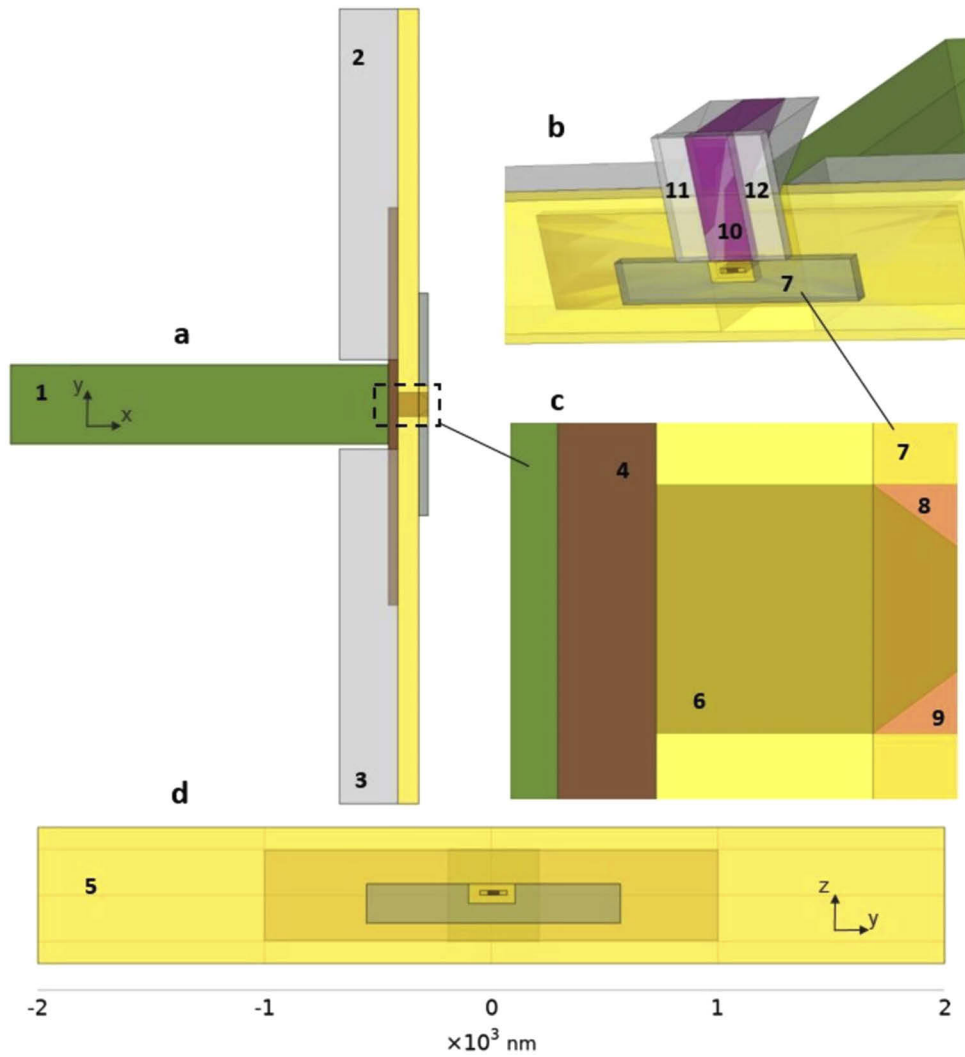
Fig. 6. (a, b, c, d) General, to-scale schematic of fully integrated photonic and plasmonic waveguides with corresponding heatsink additions and other components (numbered). Corresponding dimensions are listed in Table 3 along with material parameters in Table 4. The air-bearing (ABS) section of the MIM (7) may have a hard encasement (optional gray region) in lieu of extended Au or Au alloy. The entire structure is cladded in SiO$_2$.

Table 3. Photonic and plasmonic waveguide dimensions.

Waveguide Dimensions (*Plasmonic waveguide components are built symmetrically around SiO$_2$ insulator core*)	
SiN waveguide length, width, height (x, y, z)	2 µm, 400 nm, 400 nm placed at y = -190 nm and z = -200 nm [1]
Rear heatsink (Au) sections	310 nm, 1.785 µm, 590 nm placed at z = -295 nm [2, 3]
Antireflective trench	50 nm, 2 µm, 390 nm placed at z = -200 nm [4]
MIM rear section	110 nm, 4 µm, 590 nm placed at z = -295 nm [5]
Insulator (SiO$_2$)	160 nm, 120 nm (untapered section), 18 nm placed at z = 2 nm and **centered in y-direction** [6]
MIM front section	50 nm, 1.12 µm, 170 nm placed at z = -120 nm [7]
Au tapered/alloyed region	50 nm, 35 nm, 18 nm placed at z = 2 nm [8, 9]
Write Pole length, width	50 nm, 205 nm, 500 nm placed at z = 50 nm [10]
Adjacent heatsinks (Au) to Write Pole	50 nm, 120 nm, 500 nm [11, 12]
Tapered Write Pole and adjacent heatsink sections (x,z)	410 nm, 240 nm placed at z = 300 nm

Table 4. Film thicknesses and parameters used in optical/thermal simulations.

Film (thickness)	Refractive Index (830 nm)	Heat Capacity (J·m^{-3}K^{-1})	Thermal Conductivity (W·m^{-1}K^{-1})
Heated Air + Lubricant mixture[17,18]*(4.0 nm)*	2.9 + 0.12	2.0×10^6	1.0
Carbon Overcoat (5.0 nm)	1.32 + 0.0021i	2.0×10^6	3.0
FePt (9 nm)	3.04 + 2.69i	3.3×10^6	5.7, 1.14 in-plane
MgO (7 nm)	1.65	3.36×10^6	1.6
Amorphous Underlayer (9 nm)	3.72 + 3.99i	3.06×10^6	10.5
Heat Sink (72 nm)	5.87 + 4.68i	2.15×10^6	70
Materials (NFT, waveguide)			
Gold	0.06 + 5.17i	2.49×10^6	140
SiO$_2$	1.4	2.2×10^6	1.25
SiN	2.0	2.34×10^6	30
Write Pole	3.0 + 4.0i	3.73×10^6	15.0

The micromagnetic results in Fig. 5 are obtained from a stochastic LLB equation as outlined in Ref. [35] where simulations were shown to have good agreement with the mean-field atomistic LLG–Langevin treatment [27]. The temperature data used to determine the relaxation rates for the LLB equation are retrieved from the steady state solution of the thermal diffusion simulation and extracted from the center of the recording layer. The micromagnetic results are then convolved with the reciprocity field of the magnetic reader to produce a voltage signal in the time domain. A Fourier transform of the convolution yields the power spectrum from which the signal to noise ratio (SNR) was determined as shown in Fig. 5(a). The SNR and jitter are computed along the micro-tracks with a linear density of 300 kfci (1 kfci = 1 kbpi), head speed of 2000 cm/s, and a coil current of 65 mA around the write pole with only the best values (highest SNR and lowest jitter) reported. The SNR is defined as 10×log (signal/noise power) while the magnetic write width (MWW) is the full width half max of the signal, and the jitter is the standard deviation of the (bit length)/√2 [36]. Material parameters used within the micromagnetic simulations are outlined in Table 5.

Table 5. Parameters used in micromagnetic simulations.

Parameter	Mean	Standard Deviation	Other
Grain Diameter	6.24 nm	2.63 nm	
Curie Temperature, Tc	659 K	17 K	
Hk(0)	70.3 kOe	12.1 kOe	$Hk(T)/Hk(0) = (1-T/Tc)^{0.3564}$
Gilbert's Damping			0.05

4. Conclusion

To conclude, we have investigated a MIM-NFT for HAMR that is suitable for direct coupling from a photonic waveguide. The direct coupling of the optical field and heat generation within this design is able to primarily trap energy in the insulator core [15], thereby helping to minimize parasitic heating effects in the NFT. Furthermore, the size of the heated region may be manipulated by pulsing input power or reducing the size of the insulator layer rather than reducing the size of the thin-film Au [17,34] which would otherwise reduce the overall thermal conductivity of the structure. The modelling shows that use of Au alloys has the potential to benefit the device, in particular to increase the hardness of the NFT at the ABS surface and if larger thermal gradients are desired in the recording medium [19,25]. In addition, micromagnetic simulations show very good performance parameters with minimum jitters of approximately 2.0 nm when bit writing, along with very good SNR of 16 dB for HAMR devices and sufficient MWWs of roughly 40 nm in order to meet industry standards for recording density. Such nanoresonator designs that are able to produce the reported thermal gradients have also been proposed for use in data recording technologies that use spin-transfer torque or for quantum information processing which may require strongly driven systems [34,37–39].

Disclosures

The authors declare no conflicts of interest.

References

1. N. Abadía, F. Bello, C. Zhong, P. Flanigan, D. M. McCloskey, C. Wolf, A. Krichevsky, D. Wolf, F. Zong, A. Samani, D. V. Plant, and J. F. Donegan, "Optical and thermal analysis of the light-heat conversion process employing an antenna-based hybrid plasmonic waveguide for HAMR," Opt. Express **26**(2), 1752–1765 (2018).
2. W. A. Challener, C. Peng, A. V. Itagi, D. Karns, W. Peng, Y. Peng, X. Yang, X. Zhu, N. J. Gokemeijer, Y. T. Hsia, G. Ju, R. E. Rottmayer, M. A. Seigler, and E. C. Gage, "Heat-assisted magnetic recording by a near-field transducer with efficient optical energy transfer," Nat. Photonics **3**(4), 220–224 (2009).
3. B. C. Stipe, T. C. Strand, C. C. Poon, H. Balamane, T. D. Boone, J. A. Katine, J.-L. Li, V. Rawat, H. Nemoto, A. Hirotsune, O. Hellwig, R. Ruiz, E. Dobisz, D. S. Kercher, N. Robertson, T. R. Albrecht, and B. D. Terris, "Magnetic recording at 1.5 Pb m−2 using an integrated plasmonic antenna," Nat. Photonics **4**(7), 484–488 (2010).
4. H. T. Miyazaki and Y. Kurokawa, "Squeezing Visible Light Waves into a 3-nm-Thick and 55-nm-Long Plasmon Cavity," Phys. Rev. Lett. **96**(9), 097401 (2006).

5. C. Zhong, P. Flanigan, N. Abadía, F. Bello, B. D. Jennings, G. Atcheson, J. Li, J.-Y. Zheng, J. J. Wang, and R. Hobbs, "Effective heat dissipation in an adiabatic near-field transducer for HAMR," Opt. Express **26**(15), 18842–18854 (2018).

6. A. Datta and X. Xu, "Comparative study of optical near-field transducers for heat-assisted magnetic recording," Opt. Eng. **56**(12), 121906 (2017).

7. D. Weller, G. Parker, O. Mosendz, A. Lyberatos, D. Mitin, N. Y. Safonova, and M. Albrecht, "Review Article: FePt heat assisted magnetic recording media," *Journal of Vacuum Science & Technology B, Nanotechnology and Microelectronics: Materials, Processing Measurement, and Phenomena*, 34 (2016).

8. V. Krishnamurthy, D. Keh Ting Ng, Z. Cen, B. Xu, and Q. Wang, "Maximizing the Plasmonic Near-Field Transducer Efficiency to Its Limit for HAMR," J. Lightwave Technol. **34**(4), 1184–1190 (2016).

9. K.-T. Lee, S. Seo, J. Y. Lee, and L. J. Guo, "Ultrathin metal-semiconductor-metal resonator for angle invariant visible band transmission filters," Appl. Phys. Lett. **104**(23), 231112 (2014).

10. H. Yang, J. Li, and G. Xiao, "Decay and propagation properties of symmetric surface plasmon polariton mode in metal–insulator–metal waveguide," Opt. Commun. **395**, 159–162 (2017).

11. W. M. Abbott, C. P. Murray, C. Zhong, C. Smith, C. McGuinness, E. Rezvani, C. Downing, D. Daly, A. K. Petford-Long, F. Bello, D. McCloskey, and J. F. Donegan, "Less is More: Improved Thermal Stability and Plasmonic Response in Au Films via the Use of SubNanometer Ti Adhesion Layers," ACS Appl. Mater. Interfaces **11**(7), 7607–7614 (2019).

12. N. Bodenschatz, A. Liemert, S. Schnurr, U. Wiedwald, and P. Ziemann, "Extending the 3ω method: Thermal conductivity characterization of thin films," Rev. Sci. Instrum. **84**(8), 084904 (2013).

13. J. Chen, G. A. Smolyakov, S. R. J. Brueck, and K. J. Malloy, "Surface plasmon modes of finite, planar, metal-insulator-metal plasmonic waveguides," Opt. Express **16**(19), 14902–14909 (2008).

14. M. Zhang and Z. Wang, "Analytical method for metal-insulator-metal surface plasmon polaritons waveguide networks," Opt. Express **27**(1), 303–321 (2019).

15. A. Krichevsky, C. B. Wolf, F. D. Bello, K. E. Ballantine, J. Donegan, and D. M. O. McCloskey, "Method and system for reducing undesirable reflections in a HAMR write apparatus," US Patent 9484051, 2016.

16. H. Choo, M.-K. Kim, M. Staffaroni, T. J. Seok, S. Cabrini, P. J. Schuck, M. C. Wu, and E. Yablonovitch, "Nanofocusing in a metal–insulator–metal gap plasmon waveguide with a three-dimensional linear taper," Nat. Photonics **6**(12), 838–844 (2012).

17. A. Krichevsky, F. Bello, C. Wolf, F. Zong, D. Wolf, D. McCloskey, K. Ballantine, and J. Donegan, "Architecture for metal-insulator-metal near-field transducer for heat-assisted magnetic recording," US Patent 10249336, 2019.

18. A. Krichevsky, F. Bello, C. Wolf, F. Zong, D. Wolf, D. McCloskey, K. Ballantine, and J. Donegan, "Metal-insulator-metal near-field transducer for heat-assisted magnetic recording," US Patent 10360939, 2019.

19. N. Zhou, X. Xu, A. T. Hammack, B. C. Stipe, K. Gao, W. Scholz, and E. C. Gage, "Plasmonic near-field transducer for heat-assisted magnetic recording," Nanophotonics **3**(3), 141–155 (2014).

20. O. K. Orhan and D. D. O'Regan, "Plasmonic performance of $Au_xAg_yCu_{1-x-y}$ alloys from many-body perturbation theory," J. Phys.: Condens. Matter **31**(31), 315901 (2019).

21. C. Birleanu, M. Pustan, V. Merie, R. Müller, R. Voicu, A. Baracu, and S. Craciun, "Temperature effect on the mechanical properties of gold nano films with different thickness," IOP Conf. Ser.: Mater. Sci. Eng. **147**, 012021 (2016).

22. H. J. Richter, C. C. Poon, G. Parker, M. Staffaroni, O. Mosendz, R. Zakai, and B. C. Stipe, "Direct measurement of the thermal gradient in heat assisted magnetic recording," IEEE Trans. Magn. **49**(10), 5378–5381 (2013).

23. I. Gilbert, D. A. Saunders, P. Czoschke, Z. Liu, S. Granz, and T. Rausch, "Measuring cross-track thermal gradient in heat-assisted magnetic recording," IEEE Trans. Magn. **55**(12), 1–5 (2019).

24. D. A. Saunders, J. Hohlfeld, X. Zheng, T. Rausch, and C. Rea, "HAMR thermal gradient measurements and analysis," IEEE Trans. Magn. **53**(2), 1–5 (2017).

25. O. K. Orhan, F. Bello, J. F. Donegan, and D. D. O'Regan, "Engineering Au-based alloys for high-power near-field transducers for heat-assisted magnetic recording media", To be published, 2020.

26. M.-N. Abdallah, T. Lou, J.-M. Retrouvey, and S. Suri, "20 - Biomaterials used in orthodontics: brackets, archwires, and clear aligners," in *Advanced Dental Biomaterials*, Z. Khurshid, S. Najeeb, M. S. Zafar, and F. Sefat, eds. (Woodhead Publishing, 2019), pp. 541–579.

27. M. Tzoufras and M. K. Grobis, "Dynamics of single-domain magnetic particles at elevated temperatures," New J. Phys. **17**(10), 103014 (2015).

28. J. Zhu and H. Li, "Understanding signal and noise in heat assisted magnetic recording," IEEE Trans. Magn. **49**(2), 765–772 (2013).

29. G. Ju, Y. Peng, E. K. Cheng, Y. Ding, A. Q. Wu, X. Zhu, Y. Kubota, T. J. Klemmer, H. Amini, L. Gao, and Z. Fan, "High density heat-assisted magnetic recording media and advanced characterization-progress and challenges," IEEE Trans. Magn. **51**(11), 1–9 (2015).

30. Y. Jiao, Y. Wang, and R. H. Victora, "A study of SNR and BER in heat-assisted magnetic recording," IEEE Trans. Magn. **51**(11), 1–4 (2015).

31. D. Suess, C. Vogler, C. Abert, F. Bruckner, R. Windl, L. Breth, and J. Fidler, "Fundamental limits in heat-assisted magnetic recording and methods to overcome it with exchange spring structures," J. Appl. Phys. **117**(16), 163913 (2015).

32. H. Li, B. Johnson, M. Morelli, M. Gibbons, and J.-G. Zhu, "Analysis of signal-to-noise ratio impact in heat assisted magnetic recording under insufficient head field," J. Appl. Phys. **117**(17), 17D133 (2015).

33. COMSOL MultiphysicsTM v.5.4 www.comsol.com. COMSOL AB, Sweden.

34. F. Bello, S. Sanvito, O. Hess, and J. F. Donegan, "Shaping and storing magnetic data using pulsed plasmonic nanoheating and spin-transfer torque," ACS Photonics **6**(6), 1524–1532 (2019).

35. D. A. Garanin, "Fokker-Planck and Landau-Lifshitz-Bloch equations for classical ferromagnets," Phys. Rev. B **55**(5), 3050–3057 (1997).

36. H. Oezelt, A. Kovacs, J. Fischbacher, S. Bance, M. Gubbins, and T. Schrefl, "Transition jitter in heat-assisted magnetic recording by micromagnetic simulation," IEEE Trans. Magn. **53**(11), 1–5 (2017).

37. M. Hensen, T. Heilpern, S. K. Gray, and W. Pfeiffer, "Strong coupling and entanglement of quantum emitters embedded in a nanoantenna-enhanced plasmonic cavity," ACS Photonics **5**(1), 240–248 (2018).

38. H. Groß, J. M. Hamm, T. Tufarelli, O. Hess, and B. Hecht, "Near-field strong coupling of single quantum dots," Sci. Adv. **4**(3) 4, eaar4906 (2018).

39. F. Bello, N. Kongsuwan, J. F. Donegan, and O. Hess, "Controlled cavity-free, single-photon emission and bipartite entanglement of near-field-excited quantum emitters," *Nano Lett.* (2020).